Article

Refractive Index Sensing Based on Multiple Fano Resonances in a Split-Ring Cavity-Coupled MIM Waveguide

Jianfeng Chen [1,2,3], Hao Yang [1,2,3], Zhiyuan Fang [1,2,3], Ming Zhao [1,3] and Chenbo Xie [1,3,*]

1   Key Laboratory of Atmospheric Optics, Anhui Institute of Optics and Fine Mechanics,
    Chinese Academy of Sciences, Hefei 230031, China; jianfengchen1212@mail.ustc.edu.cn (J.C.);
    yh9599@mail.ustc.edu.cn (H.Y.); fangzhy@mail.ustc.edu.cn (Z.F.); zhaom@aiofm.ac.cn (M.Z.)
2   Science Island Branch of Graduate School, University of Science and Technology of China,
    Hefei 230026, China
3   Advanced Laser Technology Laboratory of Anhui Province, Hefei 230037, China
*   Correspondence: cbxie@aiofm.ac.cn; +86-151-5597-3263

Abstract: A metal–insulator–metal (MIM) waveguide consisting of a circular split-ring resonance cavity (CSRRC) and a double symmetric rectangular stub waveguide (DSRSW) is designed, which can excite quadruple Fano resonances. The finite element method (FEM) is used to investigate influences of geometric parameters on the transmission characteristics of the structure. The results show that Fano resonances are excited by the interference between the DSRSW and the CSRRC. Among them, the resonance wavelengths of the Fano resonances are tuned by the narrow-band discrete state excited by the CSRRC, and the resonance line transmittance and profiles are tuned by the wide-band continuous state excited by the DSRSW. The sensitivity (S) can be up to 1328.8 nm/RIU, and the figure of merit (FOM) can be up to 4.80×10^4. Based on these advantages, the structure has potential applications in sensing in the sub-wavelength range.

Keywords: quadruple Fano resonances; MIM waveguide; sensing characteristics; independent tuning

1. Introduction

Fano resonance originates from the mutual coupling between the discrete state and the continuous state in the system [1–3]. Within a certain optical frequency range, quantum interference cancellation occurs between the two states, and the system shows a narrow optical response and high local field enhancement. Fano resonance is very sensitive to geometric parameters and medium environment, which makes it used in sensors [4–6], slow light devices [7–10] and other fields [11–14]. On the other hand, in the sub-wavelength range, the surface plasmon polaritons (SPPs) can break through the traditional optical diffraction limitation, which brings infinite possibility to the future of photonic devices [15–17]. SPPs are generated by the interaction between free electrons and incident photons on the metal surface, and propagate along the metal interface. Among many waveguide devices based on SPPs, the metal–insulator–metal (MIM) optical waveguide has a compact structure and low cost, which can easily materialize the miniaturization of the detection device and realize the transmission of nanoscale optical information. Not only that, MIM optical waveguides have also been designed for different applications, including filters [18,19], wavelength division multiplexers [20,21], couplers [22–24], and Bragg reflectors [25–27]. In these studies, a large number of Fano resonance structures based on MIM optical waveguides have been reported [28–33]. For example, a T-shaped cavity with multiple metal nanorod defects coupled to an MIM waveguide that can be used as a temperature sensor was designed by Chou et al. [34]. The transmittance and sensitivity of the Fano resonance in this structure were dependent on the geometric parameters of the uneven metal nanorod defects inside the T-shaped cavity. A simple rectangular cavity refractive index nano sensor was designed by Guo et al. [35]. This rectangular ring cavity could meet the requirements

of some special-sized devices by changing the horizontal or vertical dimensions individually. At the same time, the excited double Fano resonances could be independently tuned when the geometric sizes are changed. Yang et al. proposed a cross-shaped cavity MIM waveguide structure that could excite triple Fano resonance [36]. By independently tuning the geometric parameters of the cross-shaped cavity, the wavelength and direction of the Fano resonant peak could be easily changed. Liu et al. proposed an MIM waveguide structure composed of a D-shaped cavity and a bus waveguide with a silver barrier for human hemoglobin detection [37]. An MIM waveguide structure that can be used in refractive index sensors and slow-light devices was proposed by Chen et al. [38]. The sensitivity of this structure is 1180 nm/RIU, the FOM is 5585.3, and it can also produce a maximum optical delay of approximately 0.128 ps. Butt et al. developed a new racetrack integrated circular cavity based on an MIM waveguide for refractive index sensing [39]. The best sensitivity and FOM of the device are 1400 nm/RIU and 12.01, respectively. Palzvan et al. proposed a pressure sensor composed of two MIM waveguides and a double ring resonator, with a sensitivity of 16.5 nm/MPa, suitable for biological and biomedical engineering [40]. After that, by increasing the pressure, the resonator is further deformed into a new structure, and the sensitivity is improved to 24 nm/MPa [41]. At the same time, some sensors with higher sensitivity and wider applicability have also been designed. Palermo et al. developed a high-throughput, high-precision surface-enhanced Raman spectroscopy (SERS) nano-biosensor for effective pathogen detection, which can detect the smallest virus at a concentration of 13 pg/mL [42]. Shaltout et al. modified the principle of Fabry–Pérot interferometry so that the nanocavity with embedded metasurface can support the independent adjustable resonance of multiple bands. The high spatial resolution color filtering and spectral imaging are demonstrated through experiments in a 100 nm nanocavity [43]. Giuseppe Emanuele Lio et al. used a new technique to improve the resolution of two-photon direct laser writing lithography. Compared with the standard direct laser writing method, the size is reduced by 89% and 50% [44]. It can be seen that the double and multiple Fano resonances excited by the above structures can be used in a variety of sensors. However, the existing structures that can excite multiple Fano resonances have some defects in tunable flexibility. The flexible tuning of multiple Fano resonances is of great significance for the applications of MIM optical waveguide structures. This may be beneficial to the development of multiple Fano resonances excited by MIM waveguide devices in the field of sensing.
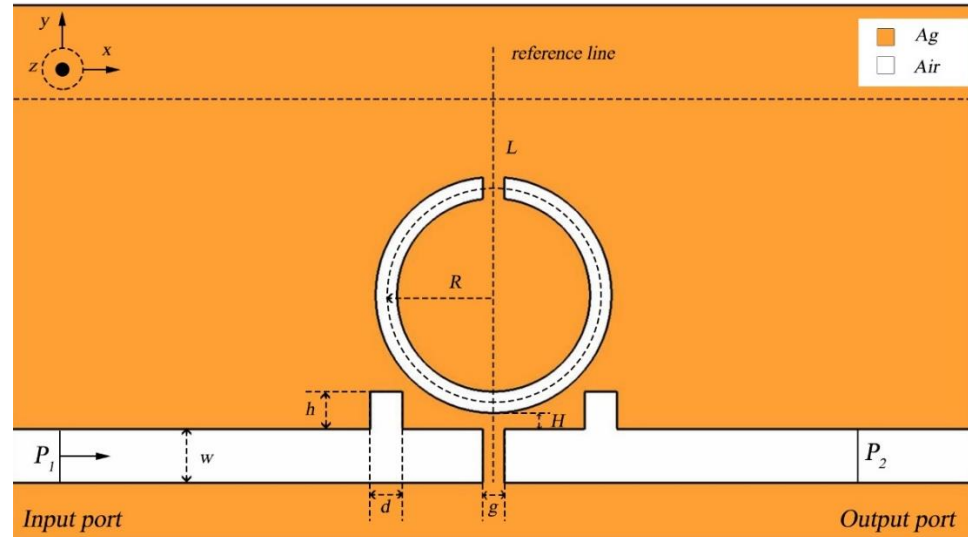
In this paper, an MIM waveguide structure consisting of a double symmetric rectangular stub waveguide (DSRSW) and a circular split-ring resonance cavity (CSRRC) is proposed to achieve quadruple Fano resonances. The split breaks the symmetry of the ring resonance cavity of the CSRRC. The influences of some geometric parameters, such as the opening width of the CSRRC, the width of the silver baffle and the width of stubs in the DSRSW, on the Fano resonances are investigated. After optimizing the geometric parameters of the structure, a better sensitivity and FOM are obtained. At the same time, the rectangular stubs added to the straight waveguide and the split openings in the ring cavity provide more feasibility for manufacturing a new type of plasma micro-nano refractive index sensor.

2. Structure and Method

The schematic diagram of the waveguide structure that consists of a CSRRC and a DSRSW is shown in Figure 1. In order to simplify the calculation, the structure is assumed to be long enough in the Z-axis direction and can be regarded as a two-dimensional structure. The overall structure is symmetrical with respect to the reference line, and the orange area represents silver and the white area represents air. The relative dielectric constant of air $\varepsilon_d = 1$, and the relative dielectric constant of silver is defined by the Debye–Drude dispersion model [45,46]:

$$\varepsilon(\omega) = \varepsilon_\infty + \frac{\varepsilon_s - \varepsilon_\infty}{1 + i\tau\omega} + \frac{\sigma}{i\omega\varepsilon_0} \qquad (1)$$

where $\varepsilon_s = -9530.5$ is the static permittivity, $\varepsilon_\infty = 3.8344$ is the dielectric constant of infinite, $\sigma = 1.1486 \times 10^7$ s/m is the conductivity of silver, $\tau = 7.35 \times 10^{-15}$ s is the relaxation time, and ω is the angular frequency of the input wave. L and R are the split length and radius of the CSRRC, and h and d are the height and width of the rectangular stubs, respectively. H is the coupling gap height, and g is the width of the silver baffle.

Figure 1. Schematic diagram of the MIM waveguide structure consisting of a DSRSW and a CSRRC.

In the Fano resonance system, the dipole moment of the discrete state is almost zero, which cannot be effectively coupled with the incident light wave. Therefore, only when the resonance condition is satisfied is there stable standing wave transmission in the waveguide structure. The resonance wavelength is determined by [38,40]:

$$\lambda = \frac{2Re(n_{eff})l_1}{m - \phi/2\pi}, \ m = 1, \ 2, \ 3 \ \ldots, \quad (2)$$

where φ is the phase shift caused by light reflection in the resonance cavity, m is the mode order of the resonance, l_1 is the length of the resonance cavity, and $Re\ (n_{eff})$ is the real part of the effective refractive index. In this paper, the finite element method (FEM) is used to analyze the optical transmission characteristics of the structure. Perfect matched layer (PML) is used to design the refractive index of air, the relative dielectric constant of silver, and the structural parameters. The fine triangular meshes are selected to ensure the perfect segmentation of the simulation area, and the maximum triangular mesh size is 10 nm. The transmittance is T = $(S_{21})^2$, where S_{21} is the transmission coefficient from the input terminal (P_1) to the output terminal (P_2). The calculation parameters are shown in Table 1. It is worth emphasizing that the bus waveguide width is fixed to 50 nm to ensure that only the fundamental transverse magnetic mode (TM$_0$) exists in the input SPP wave.

Table 1. Summary of calculated structural parameters.

| Parameter	Symbol	Quantity	Unit
Bus waveguide width	w	50	nm
Coupling gap height	H	5	nm
Split length	L	20	nm
Radius	R	100	nm
Silver baffle width	g	20	nm
Rectangular stubs height	h	35	nm
Rectangular stubs width	d	30	nm
Refractive index of bus waveguides	-	1	-
Refractive index of CSRRC	n	1	-

3. Results and Analysis

Firstly, we investigate the transmission characteristics of the designed structure using the parameters in Table 1. Figure 2 shows the transmission spectra of the whole structure, the single CSRRC, and the single DSRSW. As indicated by the blue line, the wide-band continuous state is excited by the single DSRSW. The red line indicates that the narrow-band discrete state is excited by the single CSRRC. Therefore, quadruple Fano resonances (FR1, FR2, FR3 and FR4) are produced by the interference between the narrow-band discrete state and the wide-band continuous state, as indicated by the black line.
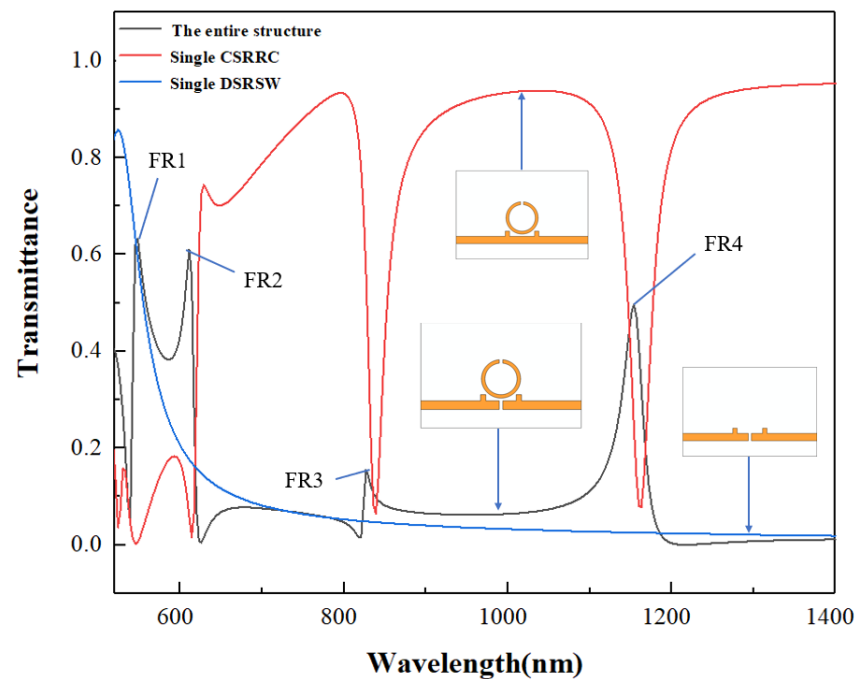
Figure 2. Transmission spectra of the single DSRSW (blue line), the single CSRRC (red line), and the entire structure (black line).

In order to better understand the Fano resonance mechanism in the structure, the magnetic field intensity distributions ($|H_z^2|$) at the four Fano resonance peaks and resonance dips are shown in Figure 3. The distribution of the magnetic field energy in the CSRRC is basically symmetrical about the reference line. From Figure 3a–d, it can be seen that most of the energy of the SPPs can be transmitted through the structure to the output port at the resonance wavelengths, while the energy of the SPPs is concentrated in the CSRRC and cannot be transmitted through the structure at the wavelengths of the Fano dips, as shown in Figure 3e–h. This is related to the transmission process of the SPPs. The SPPs enter into the DSRSW from the input port P1 and then have two transmission pathways to the output port P2. One is to transmit directly through DSRSW from P1 to P2 producing the wide-band continuous state. The other is to transmit into the CSRRC and then transmit to P2, producing the narrow-band discrete state. The two states interfere at P2, and standing waves are formed in the CSRRC when the wavelength is the resonance wavelength. When the SPPs are confined in the CSRRC, the ultra-low transmittance can be achieved. We can also understand this: When the transmission channel is in the antinode of the cavity mode, most of the energy of the SPPs is coupled to the CSRRC at the resonance wavelength, which can effectively output the coupled standing wave. On the contrary, a small amount of energy is coupled into the CSRRC, and most of the other energy propagates directly to the output port of the lower waveguide. The change in the output position of the waveguide significantly disturbs the phase of the SPPs directly coupled to itself, and the rich transmission characteristics of the structure appear. This also shows that a standing wave mode is formed when the CSRRC is at a resonant wavelength, and at a non-resonant

wavelength, the CSRRC exhibits light trapping similar to a standing wave. Moreover, the energy of the magnetic field in Figure 3a–d is higher than that in Figure 3e–h. This means that more SPPs are coupled into the CSRRC to enhance interference.
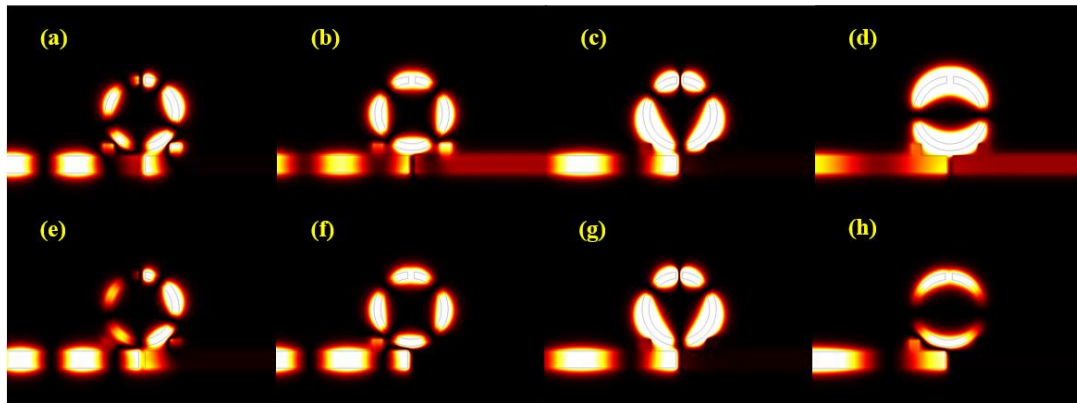

Figure 3. (**a–h**) The distributions of magnetic field intensity ($|Hz|^2$) at λ = 548 nm (FR1 peak), 611 nm (FR2 peak), 827 nm (FR3 peak), 1154 nm (FR4 peak), λ = 539 nm (FR1 dip), 626 nm (FR2 dip), 821 nm (FR3 dip), and 1199 nm (FR4 dip).

It can be seen from the above analysis that the sharp Fano resonance is excited when the CSRRC is coupled to the DSRSW. Next, the influences of the refractive index of the medium on the transmission characteristics of the structure are discussed. Small changes in wavelength can produce ultra-narrow transmission peaks, which can significantly improve sensing resolution. Figure 4 shows the transmission spectra of the structures with different refractive indices. The range of the refractive index is from 1.00 to 1.15, with an interval of 0.05. It can be seen that FR1, FR2, FR3, and FR4 all have a significant redshift with the increase in refractive index. Because of the sharp asymmetrical shape of Fano resonance, its resonance wavelength is highly sensitive to different refractive indices. However, the refractive index has almost no effect on the shape of the Fano resonances spectrum. As an abstract physical quantity in optics, the refractive index is usually determined by the specific medium. Therefore, some mediums to be measured, such as glucose solution and ethanol solution, can be filled into the CSRRC, and the refractive index-related properties of the mediums can be indirectly detected.
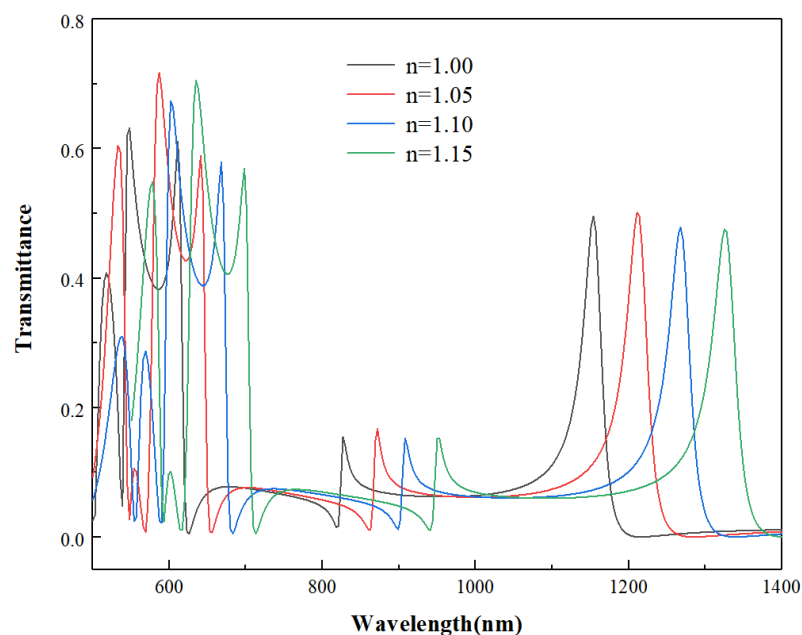
Figure 4. Transmission spectra of the waveguide structures with different refractive indices.

Two symmetric rectangular stubs are added to the straight waveguide in the proposed structure, which may affect the transmission characteristics of the structure. In the following, the influences of the stubs on the transmission characteristics are investigated. The parameters are taken from Table 1. Figure 5a shows the transmission spectra of the structure when the height of stubs changes from 25 to 35 nm with an interval of 5 nm. Figure 5b shows the transmission spectra when the width of the stubs is increased from 20 to 30 nm with an interval of 5 nm. It can be seen that although the transmittance of individual spectral lines is slightly increased, the Fano line profile and the resonance wavelengths are almost unchanged. It means that the height and width of the stubs are not suitable for adjusting the transmission spectrum or increasing the sensitivity of the structure. This also proves that the resonance wavelength is not greatly affected by the wide-band continuous state excited by the DSRSW.
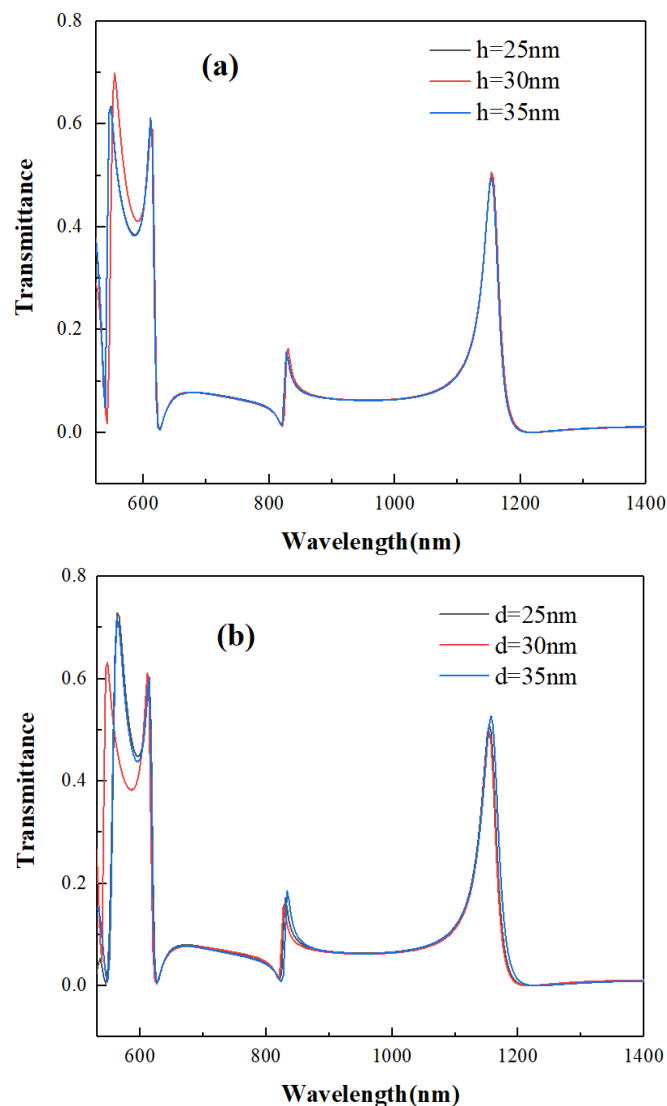
Figure 5. Transmission spectra of the structures with different (**a**) heights and (**b**) widths of the rectangular stubs.

The field energy is mostly concentrated in the CSRRC, as shown in Figure 3, so the resonance wavelength is strongly related to the geometric parameters of the CSRRC. Figure 6 shows the transmission spectra of the structures with different CSRRC opening widths. The opening width is increased from 10 to 30 nm with an interval of 5 nm. As can be seen from Figure 6a, FR1 and FR3 have an obvious blueshift, and FR2 and FR4 have a slight blueshift. The fitting of the data points in Figure 6b proves that the resonance wavelength

of the Fano resonance has a good linear relationship with the CSRRC opening widths. These results show that the resonance wavelength of the Fano resonance is determined by the narrow-band discrete states excited by CSRRC.
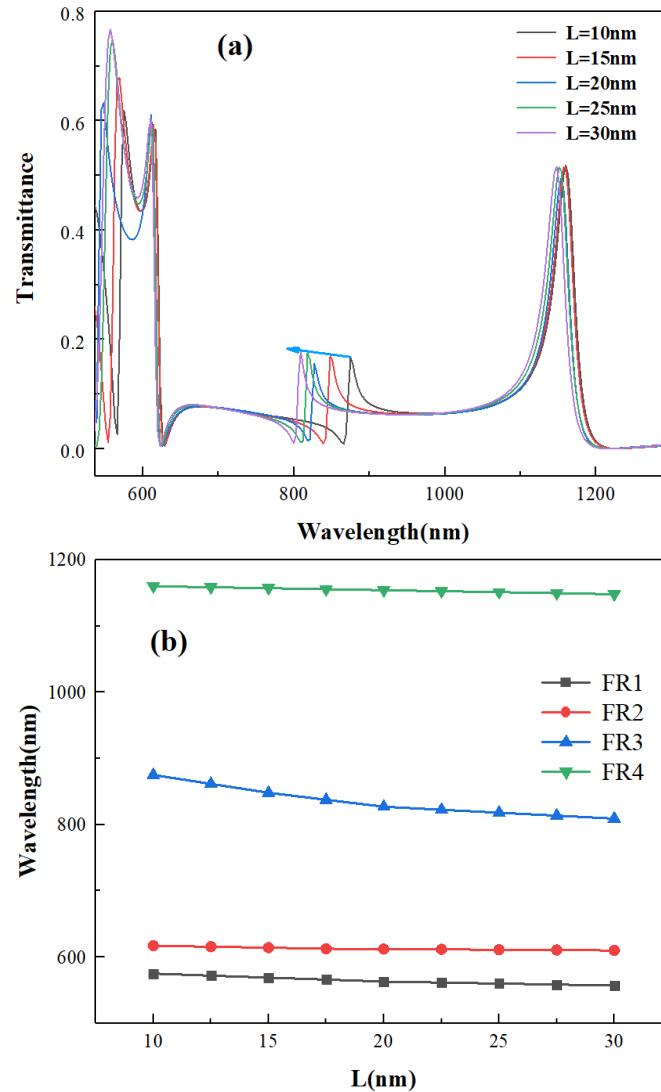
Figure 6. (**a**) Transmission spectra of the structures with different CSRRC opening widths. (**b**) The relationship between the resonance wavelength and the CSRRC opening widths.

Then, the influences of coupling distance and the width of the silver baffle on Fano resonances are also explored. Figure 7a shows the transmission spectra of the structures with different coupling distances. The coupling distance is increased from 5 to 15 nm with an interval of 5 nm. It can be seen that when the coupling distance increases, the transmittance of the resonance spectrum is significantly reduced and the Fano resonance has a slight blueshift. This is because the coupling of the narrow-band discrete state and the wide-band continuous state becomes weaker when the CSRRC is farther from the DSRSW. However, the resonance wavelengths of the Fano resonances are almost unchanged, and the profiles are roughly the same. Subsequently, the width of the silver baffle is increased from 5 to 15 nm with an interval of 5 nm. It can be seen from Figure 7b that with the increase in g, the transmittance of the resonance spectrum decreases and the Fano resonance profiles change significantly from asymmetric shapes to approximately symmetric shapes. Similarly, the resonance wavelengths of the Fano resonances are basically unchanged.
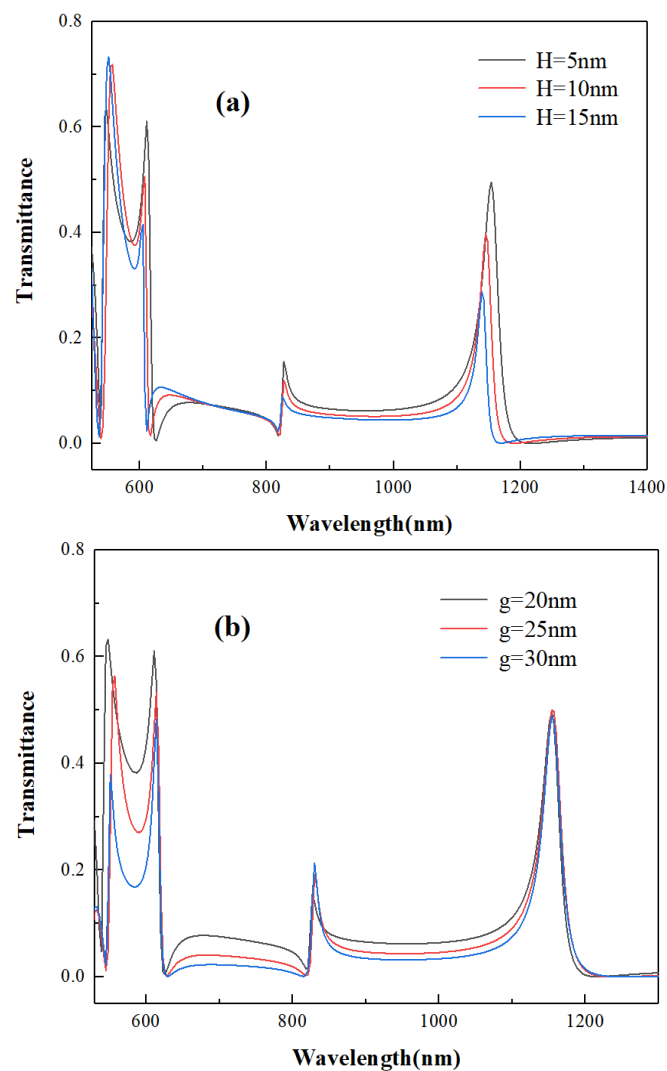
Figure 7. Transmission spectra of the structures with different (**a**) coupling distances. (**b**) Silver baffle widths.

As can be seen from the above discussion, the narrow-band discrete state in the structure is excited by the CSRRC, so the resonance wavelength of the Fano resonance is mainly determined by the geometric parameters of the CSRRC. Additionally, the wideband continuous state is excited by the DSRSW, so the transmittance and slope of the Fano resonance are mainly tuned by the parameters of the DSRSW, especially by the coupling distance and the width of the silver baffle. Next, the sensing characteristics of Fano resonances of the structure are investigated. Based on the above analysis, it can be seen that the transmittance of the structure is adjusted by g and H, and the resonance wavelength is adjusted by L. Therefore, after optimizing these parameters, it was found that the structure has the best transmittance and highest sensitivity when L = 20 nm, g = 20 nm and H = 5 nm. Figure 8 shows the relationship between the resonance wavelengths and the refractive index of the structure. Then, the least squares method is used to approximate the fitting to establish a linear regression relationship, and the linear correlation coefficients of the four Fano peaks are calculated. It can be seen that FR1, FR2, FR3, and FR4 all have good performances in the linearity, and their linear correlation coefficients are 0.9996, 0.9999, 0.9997, and 0.9994, respectively. It should be noted that the slope of the fitting straight line

represents the sensitivity. The sensitivity (S) of refractive index sensing is usually defined as the shift of the resonance wavelength ($\Delta\lambda$) per unit variation of the refractive index (Δn):

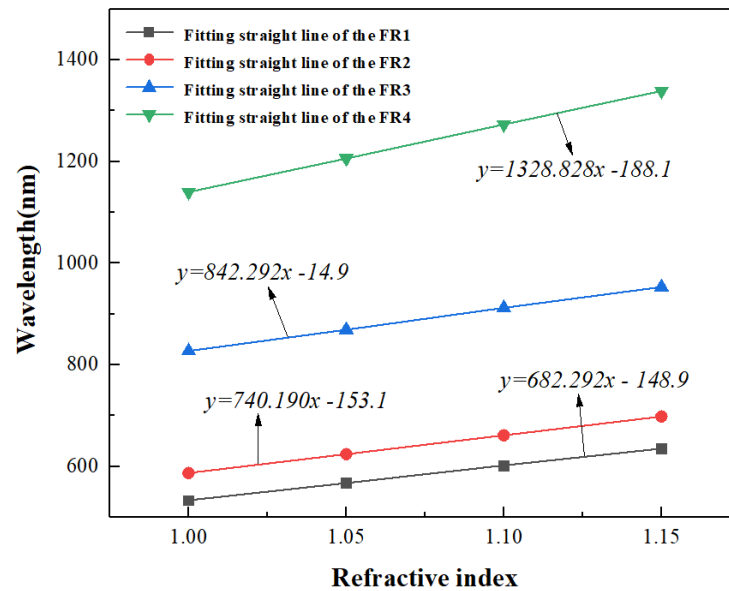$$S = \frac{\Delta\lambda}{\Delta n} \tag{3}$$

Figure 8. The relationship between the resonance wavelengths and the refractive index.

Therefore, the sensitivity levels of the structure at different resonance wavelengths are 682.3, 740.2, 842.3, and 1328.8 nm/RIU, respectively. It should be noted that, compared with FR1, FR2, and FR3, FR4 has the greatest sensitivity. From Equation (2), it can be seen that the sensitivity is proportional to l1/m. It can be seen from Figure 3 that the effective length of the resonators of FR1 and FR2 and FR3 are the same, but the order of the resonant mode of FR1 is larger. Therefore, the sensitivity of FR1 is less than FR2 and FR3. The order of the resonance modes of FR2 and FR3 are the same, but the effective length of the resonant cavity of FR2 is smaller, which means that the sensitivity of FR2 is also less than that of FR3. The effective length of the resonant cavity of FR4 is the largest, and the resonance mode is the lowest, so the sensitivity of FR4 is the largest. The comparison of the sensitivity with other published papers is shown in Table 2 [11,13,14,29,30,32,40].

Table 2. Comparison of the sensitivity with other references.

Waveguide Structure	Sensitivity	Reference
A groove and a ring resonator coupled with an MIM waveguide	1160 nm/RIU	[11]
MIM waveguide structure consisting of an M-type cavity and a baffle	780 nm/RIU	[13]
A half-ring resonator coupled MIM waveguide structure	753 nm/RIU	[14]
An end-coupled ring-groove joint MIM waveguide structure	1050 nm/RIU	[29]
MIM structure with one rectangular and two square nanorod array resonators	1090 nm/RIU	[30]
MIM structure with two concentric double-square resonators	1380 nm/RIU	[32]
A new racetrack integrated circular cavity based on MIM waveguide	1400 nm/RIU	[40]
This paper	1328.8 nm/RIU	

Furthermore, the figure of merit (FOM) is another key factor to describe the sensing performance:

$$FOM = \left(\left| \frac{dT(\lambda)/dn(\lambda)}{T(\lambda)} \right| \right) \tag{4}$$

where T is the transmission of the structure and ΔT is the relative transmission variation (induced by the refractive index change Δn) at a fixed wavelength. Figure 9 shows the FOM of the designed structure. The maximum FOM can reach up to 4.80×10^4 due to the sharp Fano resonance and ultra-low transmission at the wavelength of 1217 nm. It can be seen from the above results that the sensitivity and FOM depend on the refractive index of the medium and the geometric parameters of the structure, respectively.
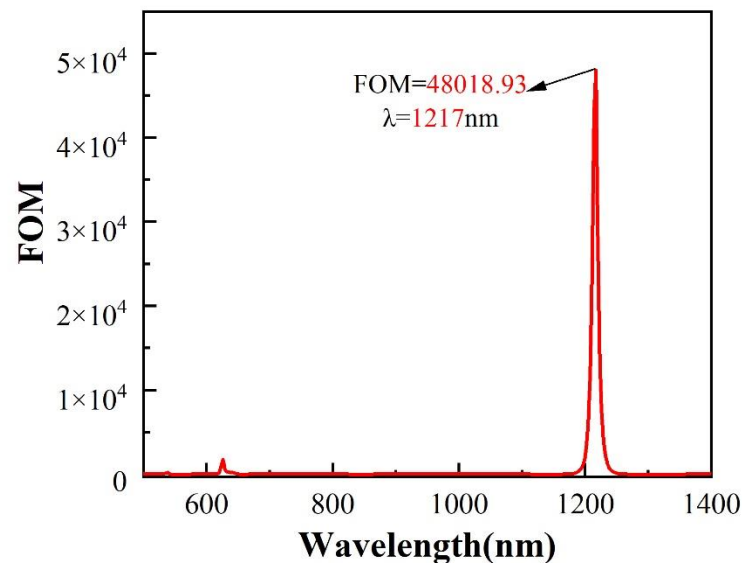

Figure 9. FOM of the designed structure.

4. Conclusions

In conclusion, a multi-geometric parameter MIM waveguide with a CSRRC and a DSRSW is designed. The simulation results show that the quadruple Fano resonances are excited in the structure. The Fano resonances are formed by the interference between the narrow-band discrete state excited by the CSRRC and the wide-band continuous state excited by the DSRSW. The transmission characteristics of the Fano resonances can be independently tuned by the geometric parameters of the structure. The change of geometric parameters will cause a certain red shift or blue shift of the transmission line of the Fano resonance. Among them, the resonance wavelengths are tuned by the opening width of the CSRRC, and the transmittance and profile are mainly tuned by the width of the silver baffle in DSRSW and the coupling distance between the CSRRC and the DSRSW. After optimizing the geometric parameters of the structure, it was found through numerical simulation that the sensitivity of the structure can reach 1328.8 nm/RIU, and the FOM can reach 4.80×10^4. At the same time, when the air in CSRRC is replaced by liquids such as glucose solution or ethanol, this structure can be used for glucose concentration or ethanol temperature sensing. To sum up, this MIM waveguide structure is believed to have potential applications in the fields of nano-refractive index sensors and nano-all-optical switches. It is worth emphasizing that although the structure has more geometric parameters and more flexible tunability, it requires more accurate manufacturing technology and more complex manufacturing processes.

Author Contributions: C.X. Conceptualization, Resources, Supervision, Funding acquisition. J.C. Conceptualization, Methodology, Software, Investigation, Data curation, Writing—original draft, Writing—review and editing. M.Z., H.Y., Z.F. Visualization. All authors have read and agreed to the published version of the manuscript.

Data Availability Statement: The data presented in this study are available on request from the author.

Conflicts of Interest: The authors declare that they have no known competing financial interests or personal relationships that could have appeared to influence the work reported in this paper.

References

1. Barnes, W.L.; Dereux, A.; Ebbesen, T.W. Surface plasmon subwavelength optics. *Nature* **2003**, *424*, 824–830. [CrossRef]
2. Tao, J.; Huang, X.G.; Lin, X.; Zhang, Q.; Jin, X. A narrow-band subwavelength plasmonic waveguide filter with asymmetrical multiple-teeth-shaped structure. *Opt. Express* **2009**, *17*, 13989–13994. [CrossRef]
3. Wahsheh, R.A.; Lu, Z.; Abushagur, M.A.G. Nanoplasmonic couplers and splitters. *Opt. Express* **2009**, *17*, 19033–19040. [CrossRef] [PubMed]
4. Luk'Yanchuk, B.; Zheludev, N.; Maier, S.; Halas, N.; Nordlander, P.; Giessen, H.; Chong, C.T. The Fano resonance in plasmonic nanostructures and metamaterials. *Nat. Mater.* **2010**, *9*, 707–715. [CrossRef] [PubMed]
5. Cai, D.-J.; Huang, Y.-H.; Wang, W.-J.; Ji, W.-B.; Chen, J.-D.; Chen, Z.-H.; Liu, S.-D. Fano Resonances Generated in a Single Dielectric Homogeneous Nanoparticle with High Structural Symmetry. *J. Phys. Chem. C* **2015**, *119*, 4252–4260. [CrossRef]
6. Desrier, A.; Maquet, A.; Taïeb, R.; Caillat, J. Ionization dynamics through a Fano resonance: Time-domain interpretation of spectral amplitudes. *Phys. Rev. A* **2018**, *98*, 053406. [CrossRef]
7. Jafari, O.; Shi, W.; LaRochelle, S. Efficiency-Speed Tradeoff in Slow-Light Silicon Photonic Modulators. *IEEE J. Sel. Top. Quantum Electron.* **2020**, *27*, 1–11. [CrossRef]
8. Xie, Y.; Chai, J.; Ye, Y.; Song, T.; Liu, B.; Zhang, L.; Zhu, Y.; Liu, Y. A Tunable Slow Light Device with Multiple Channels Based on Plasmon-Induced Transparency. *Plasmonics* **2021**, *16*, 1–8. [CrossRef]
9. Eroglu, Y.S.; Anjinappa, C.K.; Guvenc, I.; Pala, N. Slow Beam Steering and NOMA for Indoor Multi-User Visible Light Communications. *IEEE Trans. Mob. Comput.* **2019**, *20*, 1627–1641. [CrossRef]
10. Kumari, S.; Kumar, A.; Medhekar, S. Slow light in rod type 2D photonic crystal waveguide comprising of cavity: Optimization and analysis. *Optik* **2021**, *231*, 166438. [CrossRef]
11. Sumetsky, M. Fundamental limit of microresonator field uniformity and slow light enabled ultraprecise displacement metrology. *Opt. Lett.* **2021**, *46*, 1656–1659. [CrossRef] [PubMed]
12. Hattori, S.; Moris, M.; Shinozaki, K.; Ishii, K.; Verbiest, T. Vortex-Induced Harmonic Light Scattering of Porphyrin J-Aggregates. *J. Phys. Chem. B* **2021**, *125*, 2690–2695. [CrossRef] [PubMed]
13. Marinkovic, D.Z.; Medar, M.L.J.; Becin, A.P.; Andric, S.A.; Kostic, T.S. Growing Up Under Constant Light: A Challenge to the Endocrine Function of the Leydig Cells. *Front. Endocrinol.* **2021**, *12*, 653602. [CrossRef]
14. Eyland, D.; van Wesemael, J.; Lawson, T.; Carpentier, S. The impact of slow stomatal kinetics on photosynthesis and water use efficiency under fluctuating light. *Plant Physiol.* **2021**, *186*, 998–1012. [CrossRef] [PubMed]
15. Yu, Z.; Chouchene, B.; Liu, M.; Moussa, H.; Schneider, R.; Moliere, M.; Liao, H.; Chen, Y.; Sun, L. Influence of laminated architectures of heterostructured CeO2-ZnO and Fe_2O_3-ZnO films on photodegradation performances. *Surf. Coat. Technol.* **2020**, *403*, 126367. [CrossRef]
16. Zhao, R.; Li, J.; Zhang, Q.; Liu, X.; Zhang, Y. Behavior of SPPs in chiral–graphene–chiral structure. *Opt. Lett.* **2021**, *46*, 1975–1978. [CrossRef]
17. Moreira, R.; Wolfe, J.; Taylor, S.D. A high-yielding solid-phase total synthesis of daptomycin using a Fmoc SPPS stable kynurenine synthon. *Org. Biomol. Chem.* **2021**, *19*, 3144–3153. [CrossRef]
18. Chen, X. Synthesis of multi-band filters based on multi-prototype transformation. *IET Microw. Antennas Propagation* **2020**, *15*, 103–114. [CrossRef]
19. Dellweg, D.; Haidl, P.; Kerl, J.; Maurer, L.; Köhler, D. Bench testing of noninvasive ventilation masks with viral filters for the protection from inhalation of infectious respirable particles. *J. Occup. Environ. Hyg.* **2021**, *18*, 118–127. [CrossRef]
20. Feng, C.; Ying, Z.; Zhao, Z.; Gu, J.; Pan, D.Z.; Chen, R.T. Wavelength-division-multiplexing (WDM)-based integrated electronic–photonic switching network (EPSN) for high-speed data processing and transportation. *Nanophotonics* **2020**, *9*, 4579–4588. [CrossRef]
21. Nguyen, V.H.; Kim, I.K.; Seok, T.J. Silicon Photonic Mode-Division Reconfigurable Optical Add/Drop Multiplexers with Mode-Selective Integrated MEMS Switches. *Photonics* **2020**, *7*, 80. [CrossRef]
22. Kang, S.; Zhang, R.; Hao, Z.; Jia, D.; Gao, F.; Bo, F.; Zhang, G.; Xu, J. High-efficiency chirped grating couplers on lithium niobate on insulator. *Opt. Lett.* **2020**, *45*, 6651–6654. [CrossRef] [PubMed]
23. Liu, Y.; Huang, X.; Li, Z.; Guan, H.; Wei, Q.; Fan, Z.; Han, W.; Li, Z.-Y. Efficient grating couplers on a thin film lithium niobate–silicon rich nitride hybrid platform. *Opt. Lett.* **2020**, *45*, 6847–6850. [CrossRef] [PubMed]

24. Huang, H.; Wu, Y.; Wang, W.; Feng, W.; Shi, Y. Analysis of the Propagation Constant of a Ridge Gap Waveguide and Its Application of Dual-Band Unequal Couplers. *IEEE Trans. Plasma Sci.* **2020**, *48*, 4163–4170. [CrossRef]

25. Jin, H.; Chen, L.; Li, J.; An, X.; Wu, Y.; Zhu, L.; Yi, H.; Li, K.H. Vertically stacked RGB LEDs with optimized distributed Bragg reflectors. *Opt. Lett.* **2020**, *45*, 6671–6674. [CrossRef]

26. Lohithakshan, L.C.; Geetha, V.; Kannan, P. Single polymer-variable index for the design and fabrication of variable stop band distributed Bragg reflectors. *Opt. Mater.* **2020**, *110*, 110509. [CrossRef]

27. Wu, C.; Wei, W.; Yuan, X.; Zhang, Y.; Yan, X.; Zhang, X. Design and Simulation of Low-Threshold Miniaturized Single-Mode Nanowire Lasers Combined with a Photonic Crystal Microcavity and Asymmetric Distributed-Bragg-Reflector Mirrors. *Nanomaterials* **2020**, *10*, 2344. [CrossRef]

28. Chen, Y.; Zhou, X.; Xu, Y.; Xiao, C.; Zhu, Q. Fano Resonance Sensing Based on Coupling ofSub-wavelength Grating and All-dielectric MultilayerFilm under Angle Modulation. *Appl. Opt.* **2021**, *60*, 2902–2906. [CrossRef]

29. Nikoghosyan, H.; Manukyan, V.; Harutyunyan, S.; Nikoghosyan, G. Fano resonance model for the processes of photoionization of two-well heterostructures in a transverse electric field. *Phys. E Low-Dimensional Syst. Nanostructures* **2020**, *128*, 114587. [CrossRef]

30. Chen, Y.; Zhang, M.; Cao, J.; Xiao, C.; Zhu, Q. Structure of Multiple Fano Resonances in Double-baffle MDM Waveguide Coupled Cascaded Square Cavity for Application of High Throughput Detection. *Plasmonics* **2021**, *9*, 1–10. [CrossRef]

31. Kilic, S.C.; Kocaman, S. Highly Sensitive and Tunable Fano-Like Rod-Type Silicon Photonic Crystal Refractive Index Sensor. *IEEE Sens. J.* **2021**, *21*, 7551–7557. [CrossRef]

32. Zhu, J.; Qin, Y.; Wang, G.; Zheng, K. Novel Crescent-Shaped Cavity Resonator Based on Fano Resonance Spectrum. *Plasmonics* **2021**, *16*, 1557–1565. [CrossRef]

33. Tu, D.; Wu, Y.; Xie, J.; Zang, X.; Ding, L.; Chen, L. Switchable Fano Resonance Based on Cut-Induced Asymmetric Split-Ring Resonators with Dirac Semimetal Film. *Plasmonics* **2021**, *16*, 1405–1415. [CrossRef]

34. Chau, Y.-F.C.; Chao, C.-T.C.; Huang, H.J.; Kumara, N.T.R.N.; Lim, C.M.; Chiang, H.-P. Ultra-High Refractive Index Sensing Structure Based on a Metal-Insulator-Metal Waveguide-Coupled T-Shape Cavity with Metal Nanorod Defects. *Nanomaterials* **2019**, *9*, 1433. [CrossRef]

35. Guo, J.; Yang, X.; Wang, Y.; Wang, M.; Hua, E.; Yan, S. Refractive Index Nanosensor With Simple Structure Based on Fano Resonance. *IEEE Photonics J.* **2020**, *12*, 1–10. [CrossRef]

36. Yang, Q.; Liu, X.; Guo, F.; Bai, H.; Zhang, B.; Li, X.; Tan, Y.; Zhang, Z. Multiple Fano resonance in MIM waveguide system with cross-shaped cavity. *Optik* **2020**, *220*, 165163. [CrossRef]

37. Liu, X.; Li, J.; Chen, J.; Rohimah, S.; Tian, H.; Wang, J.; Siti, R.; Li, J. Fano resonance based on D-shaped waveguide structure and its application for human hemoglobin detection. *Appl. Opt.* **2020**, *59*, 6424–6430. [CrossRef] [PubMed]

38. Chen, J.; Li, J.; Liu, X.; Rohimah, S.; Tian, H.; Qi, D. Fano resonance in a MIM waveguide with double symmetric rectangular stubs and its sensing characteristics. *Opt. Commun.* **2020**, *482*, 126563. [CrossRef]

39. Butt, M.; Kaźmierczak, A.; Kazanskiy, N.; Khonina, S. Metal-Insulator-Metal Waveguide-Based Racetrack Integrated Circular Cavity for Refractive Index Sensing Application. *Electronics* **2021**, *10*, 1419. [CrossRef]

40. Palizvan, P.; Olyaee, S.; Seifouri, M. An Optical MIM Pressure Sensor Based on a Double Square Ring Resonator. *Photonic Sens.* **2018**, *8*, 242–247. [CrossRef]

41. Palizvan, P.; Olyaee, S.; Seifouri, M. High Sensitive Optical Pressure Sensor Using Nano-Scale Plasmonic Resonator and Metal-Insulator-Metal Waveguides. *J. Nanoelectron. Optoelectron.* **2018**, *13*, 1449–1453. [CrossRef]

42. Palermo, G.; Rippa, M.; Conti, Y.; Vestri, A.; Castagna, R.; Fusco, G.; Suffredini, E.; Zhou, J.; Zyss, J.; De Luca, A.; et al. Plasmonic Metasurfaces Based on Pyramidal Nanoholes for High-Efficiency SERS Biosensing. *ACS Appl. Mater. Interfaces* **2021**, *13*, 43715–43725. [CrossRef] [PubMed]

43. Shaltout, A.M.; Kim, J.; Boltasseva, A.; Shalaev, V.M.; Kildishev, A.V. Ultrathin and multicolour optical cavities with embedded metasurfaces. *Nat. Commun.* **2018**, *9*, 1–7. [CrossRef] [PubMed]

44. Lio, G.E.; Ferraro, A.; Ritacco, T.; Aceti, D.M.; De, A.; Giocondo, M.; Caputo, R. Leveraging on ENZ Metamaterials to Achieve 2D and 3D Hyper-Resolution in Two-Photon Direct Laser Writing. *Adv. Mater.* **2021**, *33*, 2008644. [CrossRef]

45. Lotfiani, A.; Mohseni, S.; Ghanaatshoar, M. High-sensitive optoelectronic SPR biosensor based on Fano resonance in the integrated MIM junction and optical layers. *Opt. Commun.* **2020**, *477*, 126323. [CrossRef]

46. Chen, J.; Gan, F.; Wang, Y.; Li, G. Plasmonic Sensing and Modulation Based on Fano Resonances. *Adv. Opt. Mater.* **2018**, *6*, 1701152. [CrossRef]